energies

Article

Three-Stage Modeling Framework for Analyzing Islanding Capabilities of Decarbonized Energy Communities

Tomislav Capuder *, Bojana Barać *, Matija Kostelac and Matej Krpan

Department of Energy and Power Systems, Faculty of Electrical Engineering and Computing, University of Zagreb, 10000 Zagreb, Croatia; matija.kostelac@fer.hr (M.K.); matej.krpan@fer.hr (M.K.)
* Correspondence: tomislav.capuder@fer.hr (T.C.); bojana.barac@fer.hr (B.B.)

Abstract: Contrary to microgrids (MGs) for which grid code or legislative support are lacking in the majority of cases, energy communities (ECs) are one of the cornerstones of the energy transition backed up by the EU's regulatory framework. The main difference is that, unlike MGs, ECs grow and develop organically through citizen involvement and investments in the existing low-voltage (LV) distribution networks. They are not planned and built from scratch as closed distribution systems that are independent of distribution system operator plans as assumed in the existing literature. An additional benefit of ECs could be the ability to transition into island mode, contributing to the resilience of power networks. To this end, this paper proposes a three-stage framework for analyzing the islanding capabilities of ECs. The framework is utilized to comprehensively assess and compare the islanding capabilities of ECs whose organic development is based upon three potential energy vectors: electricity, gas, and hydrogen. Detailed dynamic simulations clearly show that only fully electrified ECs inherently have adequate islanding capabilities without the need for curtailment or additional investments.

Keywords: converter-dominated power systems; dynamic stability; electrification; energy communities; islanding; low-inertia power systems; multi-energy systems; optimization

Citation: Capuder, T.; Barać, B.; Kostelac, M.; Krpan, M. Three-Stage Modeling Framework for Analyzing Islanding Capabilities of Decarbonized Energy Communities. *Energies* **2023**, *16*, 4321. https://doi.org/10.3390/en16114321

Academic Editor: Anna Pinnarelli

Received: 11 April 2023
Revised: 17 May 2023
Accepted: 22 May 2023
Published: 25 May 2023

1. Introduction

1.1. Motivation

The ever-increasing use of renewable energy sources (RESs) is encouraged and imposed by the European legislative framework. To achieve a fundamental transformation of the energy system, the current European "Clean Energy Package" places local consumers at the heart of the energy transition [1]. Its aim is to foster citizens' investment in RESs, furnishing the transition from a centralized network with passive consumers into a flexible network of active consumers [2]. Hence, rapid growth of RESs in distribution networks can be expected in the near future, which leads to new challenges in energy market reform and operation of distribution system operators (DSOs) in terms of system management and planning. The rise of consumer cooperation in (renewable) energy production creates opportunities for small-scale actors for market participation and service provision [3]. The realization of these opportunities usually relies on structures such as aggregators, virtual power plants, microgrids (MGs), and energy communities (ECs) [3].

The EC as a cornerstone of the energy transition is the focus of European research [3], enabling self-producing, self-consuming, sharing, and selling energy from distributed sources. A regulatory framework of ECs is given by the Renewable Energy Directive and the Electricity Market Directive. The EU has introduced two concepts of ECs in its legislation, i.e., Citizen Energy Communities and Renewable energy communities [4]. The primary goal of these communities is to allow citizens to collectively organize their participation in the energy system while providing a host of benefits such as local provision of ancillary services, alleviation of the need for traditional network upgrades, higher integration of RESs, market participation of end consumers, lower energy prices, and economic income for members [5]. However, national (by)laws often spatially limit ECs; for instance, the EC in Croatia is limited only to the end-users downstream of the same MV/LV substation [6]. The EC is usually managed by the community manager that has access to the data of devices and meter measurements of each community member [7]. ECs are built, sized, and managed to provide economic savings and benefits for their end-users. In this context, the possibility of islanding could be an added feature that the EC will provide to its end-users. Although islanding capability is commonly related to MGs in the literature, MGs are not consistently defined in the existing standards. In fact, only five of them (IEC 62898-1, IEC 62898-2, IEEE P2030.8, IEC 62898-3, and IEEE 1574 [8]) deal with MGs, but primarily as a power supply for remotely located systems with weak or non-existing grid connections, e.g., telecommunication systems and islands. In reality, most of MGs will not be planned and built as separate, closed distribution systems that are operated and managed independently of a DSO considering existing standards. Since the EC and islanding capability are recognized and defined in legislation, islanding as an added feature to ECs would contribute to the resilience, self-sufficiency, and energy independence of electric networks. Controllable RESs and loads in MGs and ECs reduce dependence on the main grid. If there is sufficient energy controlled in a proper way, the EC could separate and operate independently from the external grid in the case where there is an interruption of electricity supply. Therefore, islanding requires a lot of attention when talking about RES integration in MGs and ECs. Islanding can be planned, which means MG or EC disconnects from the main network in a controlled manner as it has enough electric power to reliably supply the local load. In addition, islanding can be unplanned as an undesired event caused by failures in the main grid, line tripping, etc. The objective of MG/EC planning is to ensure safe and reliable MG/EC operation for both planned and unplanned islanding. This paper aims to investigate in which cases and with which transition strategies the EC can enable islanding to its end-users.

1.2. Literature Review

In the context of islanding capability, developing an appropriate MG/EC scheduling model that can ensure reliable grid-connected and islanded operation (as well as smooth islanding transition) is of fundamental importance. There are several papers tackling this issue. Reference [9] presents the optimal scheduling of cooperative ECs, observing the energy exchange among assets within ECs as well as energy exchange with the utility grid. However, this approach ensures only reliable grid-connected operation, and the possibility of islanding is neglected. Authors in [10–17] propose different models of optimal MG scheduling for both grid-connected and islanded modes. However, the islanding constraints are based only on the energy balance ensuring that production is equal to consumption in both modes, not considering the dynamics during the transition to islanded mode. The same shortcoming can be noticed in [18–20] where the optimal reserve capacity required for successful islanding is determined. These references place emphasis on meeting frequency constraints after islanding, while voltage constraints are neglected. Moreover, the authors in [21–24] consider only the dynamic frequency behavior through limits of the maximum rate of change of frequency (RoCoF), nadir, and the steady-state frequency deviation. These limitations are derived analytically and incorporated into the MG scheduling model. Nonetheless, the voltage stability is ignored. On the other hand, the study in [25] proposes a methodology to satisfy the dynamic voltage security constraints during MG islanding and the post-islanding steady state, neglecting the dynamic frequency constraints. The authors in [26] use an AC power flow to calculate the voltages and frequency deviations and to guarantee acceptable nodal voltages and system frequency during islanded operation, while grid-connected operation and off-grid transition are not observed. Reference [27] also investigates the microgrid islanded operation, where EV flexibility is utilized to improve the frequency fluctuation and stability, while the voltage stability, as well as transient constraints, are omitted. Only islanded microgrid operation is also observed in [28], where authors derive the frequency security constraints according to hierarchical frequency control levels to optimally schedule energy and reserves. Moreover, the steady-state stability and transient stability in all operation modes are assured by AC optimal power flow (OPF) in [29], yet the voltage stability is not fully considered. The proposed model is tested on a distribution network containing conventional distributed generators, photovoltaic (PV) units, and wind turbine (WT) units. However, their dynamics and control systems are not considered when deriving transient stability constraints. A step further is made in [30] where both static and transient islanding constraints (i.e., the maximum RoCoF and the frequency nadir as transient state criteria, and the frequency deviation as a quasi-steady-state criterion) are derived considering the contribution of traditional SGs, droop-based and virtual inertia-based converters to frequency control. Notwithstanding the inclusion of transient frequency constraints, the authors assume sufficient energy storage behind the DC capacitor as well as perfect tracking of the DC-side storage device. This approach essentially eliminates any distinction between various technologies (PV, wind, battery, hydrogen, etc.). Furthermore, transient and quasi-stationary voltage constraints are not considered. In [31], a detailed representation of unit dynamic response is used to define frequency nadir constraints. However, voltage transient constraints and RoCoF constraints are not observed by the presented method. A similar approach is presented in [32], where a neural network is used to derive the nonlinear relation between system operating conditions and frequency nadir to achieve successful islanding. By this approach, realistic factors such as saturation and dead-band can be considered, yet the voltage constraints are not modeled.

1.3. Contributions and Paper Organization

Based on the literature review, the shortcomings of the state-of-the-art are as follows: (i) no papers investigate islanding capabilities of ECs based on different energy vectors; (ii) none of them comprehensively consider detailed device-level dynamics with static and dynamic constraints in a quiescent and transient state, both on-grid and off-grid. The taxonomy of existing literature and contributions of this paper with respect to the state of the art is shown in Table 1. With that in mind, the contributions of this paper can be summarized as follows:

- Three-stage framework for analyzing the capabilities of ECs to transition into island mode considering steady-state and transient voltage/frequency constraints.
- Comprehensive analysis of the capabilities of three ECs based on different energy vectors (gas, hydrogen, fully electrified) taking into account detailed device-level dynamics on the DC side of converters.

The rest of paper is organized as follows. The EC optimization and dynamic models are described in Section 2. A case study is described in Section 3. Results are discussed in Section 4. Section 5 concludes the paper.

Table 1. Comparison of the proposed three-stage modeling framework for islanding capabilities and existing models available in the literature.

Modeling Aspects	[10–17]	[18–20]	[21–24]	[25]	[26]	[27,28]	[29]	[30]	[31,32]	**This Work**
grid-connected operation	✓	✓	✓	✓	✗	✗	✓	✓	✓	✓
islanded operation	✓	✓	✓	✓	✓	✓	✓	✓	✗	✓
off-grid transition	✗	✗	✓	✓	✗	✗	✓	✓	✗	✓
steady-state constraints	✓	✓	✓	✓	✓	✓	✓	✓	✓	✓
transient nadir constraints	✗	✗	✓	✗	✓	✓	✓	✓	✓	✓
transient RoCoF constraints	✗	✗	✓	✗	✓	✗	✓	✓	✗	✓
transient voltage constraints	✗	✗	✗	✓	✓	✗	✗	✗	✗	✓
consideration of control systems	✗	✗	✗	✗	✗	✗	✗	✓	✓	✓
full consideration of dynamics	✗	✗	✗	✗	✗	✗	✗	✗	✓	✓
including virtual inertial response	✗	✗	✗	✗	✗	✗	✗	✓	✗	✓
testing on different MG/EC setups	✗	✗	✗	✗	✗	✗	✗	✗	✗	✓

2. Energy Community Modeling

Three specific EC layouts with different ways of producing heat, electricity, and storing energy are considered in this paper: (i) fully electrified EC consisting of a centralized heat pump (HP), and battery energy storage systems (BESSs) and PV units in every household (Figure 1); (ii) gas-based EC consisting of a centralized CHP unit and a boiler, and also PV units in every household (Figure 1b); (iii) hydrogen-based EC consisting of a centralized fuel cell + electrolyzer, and PV units in every household (Figure 1c). Layout (i) presents the current trend for EC architecture based on full electrification. EC layout (ii) represents traditional end-user system architecture still mostly present in today's systems, where heating is primarily provided by fossil gas. Lastly, layout (iii) represents an electrified architecture based on hydrogen technologies, considered more as a future possibility to replace natural gas as a more environmentally friendly technology. Please note that we intentionally choose to focus on one type of technology for each EC instead of mixing technologies together as we are analyzing specific technology paths toward decarbonization. This approach will provide better insight into the flexibility potential of each option separately. Finding an optimal mix of the technologies for an energy community (or collaboration of multiple ECs) is outside the scope of this paper. Devices in ECs are sized to ensure that the energy needs are met, supported by the energy production from PVs, especially in the case of heat consumption, where all energy needs must be produced locally, since it cannot be bought directly. Additionally, each EC has a different way of storing energy (BESS, heat, hydrogen). This approach makes ECs mostly autonomous while still being able to perform market arbitrage. Layouts for ECs (i) and (iii) are chosen as they do not produce local greenhouse gas emissions. However, they are indirectly responsible for emissions produced by generating electricity bought from the market. These emissions are mostly dependent on the energy mix in a given market and, following the current emission reduction trends, they will be reduced. Additionally, every EC has a PV system to reduce their electricity import, thus lowering their carbon footprint. Every EC layout can be adapted in terms of (de)centralization of different units and redesigned for satisfying local energy consumption. The proposed framework is generic enough for analyzing the islanding capabilities of an arbitrary EC layout.

The EC model consists of three stages. The first stage is the optimization problem based on the mixed-integer linear model, which is used to determine the optimal schedule of ECs from the energy balance perspective. In the second stage, a dynamic analysis of EC island transition is conducted. If the transition was not possible, new constraints are introduced to the model to ensure the feasibility of islanding. Finally, the third stage updates the first stage with constraints obtained from the second stage, providing an optimal schedule of ECs while ensuring islanding capabilities. The proposed framework is shown in Figure 2.

2.1. Optimization Model

Before introducing the model formulation, sets of devices in each EC m are defined: boilers ($\mathcal{D}_{b,m}$), CHP units ($\mathcal{D}_{c,m}$), electrolyzers ($\mathcal{D}_{e,m}$), fuel cells ($\mathcal{D}_{f,m}$), and heat pumps ($\mathcal{D}_{h,m}$). Energy storage devices are BESS ($\mathcal{D}_{\beta,m}$), heat storage ($\mathcal{D}_{\tau,m}$), and hydrogen storage ($\mathcal{D}_{\hbar,m}$).

The optimization model is a mixed-integer linear programming model which aims to minimize the operational cost of EC m, described by (1). The model is created in the Python programming language, using Gurobi solver [33]. It consists of charges for electricity and gas bought from their respective markets ($\overline{\epsilon}_{m,t}\pi^{\mathrm{E}}_t$, $\gamma_m\pi^{\mathrm{G}}$) reduced by electricity sold on the market ($\underline{\epsilon}_{m,t}\pi^{\mathrm{E}}_t$). Electricity bought from the market has an additional cost in terms of transmission and distribution charges ($\pi^{\mathrm{trans.}}$, $\pi^{\mathrm{distr.}}$) which are not present when selling electricity to the market. $z_{d,m,t}$ is the start-up cost of units.

$$\min\left\{\sum_{t\in\mathcal{T}}\left(\overline{\epsilon}_{m,t}\left(\pi^{\mathrm{E}}_t+\pi^{\mathrm{trans.}}+\pi^{\mathrm{distr.}}\right)-\underline{\epsilon}_{m,t}\pi^{\mathrm{E}}_t+\sum_{d\in\mathcal{D}_{b,m}\cup\mathcal{D}_{c,m}}z_{d,m,t}\right)+\gamma_m\pi^{\mathrm{G}}\right\} \tag{1}$$

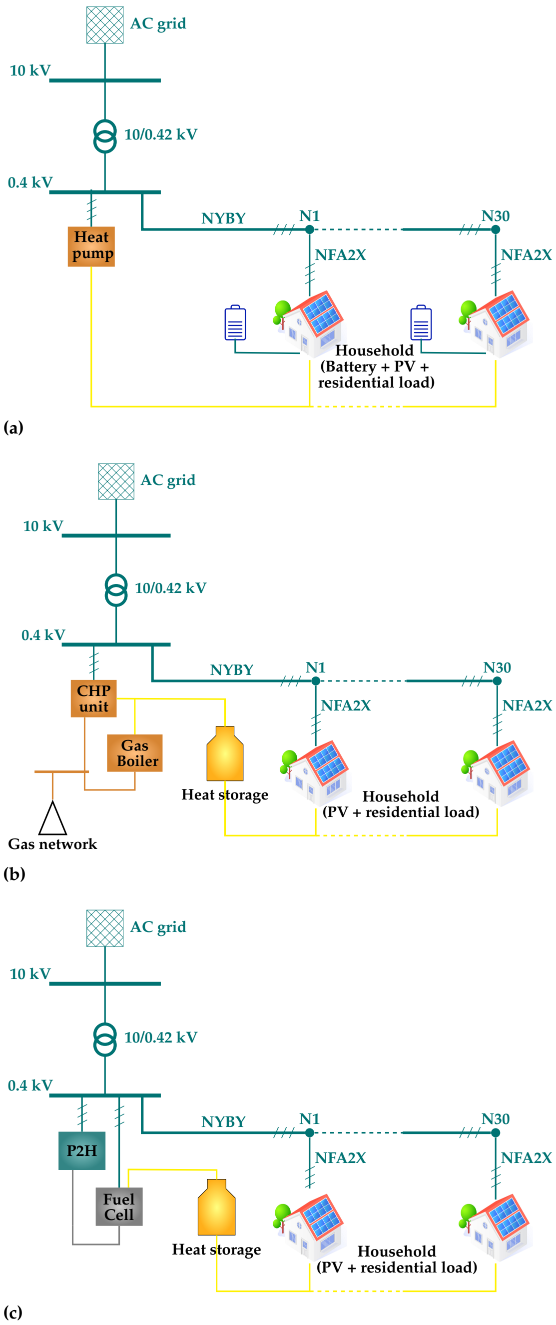

Figure 1. Layouts of observed ECs: (**a**) fully electrified EC, (**b**) gas-based EC, (**c**) hydrogen-based EC.

Input power of non-storage devices $\mathcal{D}^{C}_{m} = \mathcal{D}_{b,m} \cup \mathcal{D}_{c,m} \cup \mathcal{D}_{e,m} \cup \mathcal{D}_{f,m} \cup \mathcal{D}_{h,m}$ is limited by Equation (2). For storage devices $\mathcal{D}^{S}_{m} = \mathcal{D}_{\beta,m} \cup \mathcal{D}_{\tau,m} \cup \mathcal{D}_{\hbar,m}$, Equations (3) and (4) limit the maximum charging and discharging power; (5) prohibits simultaneous activation of charging and discharging; (6) calculates the state-of-energy at any give time step; and (7) limits the maximum and minimum available state-of-energy. All of these equations are standard in the literature and are used for most devices; thus, we did not want to repeat them for each specific device. Equation (8) models the start-up cost of boilers and CHPs through an additional binary variable $z_{d,m,t}$, which takes on value 1 if the device has started in that time step. The output power of boilers and electrolyzers is calculated by reducing the respective input power by the conversion efficiency η_d, and for HPs, the coefficient of performance is used, represented by the same symbol (η_d) for simplicity (9). Since the CHP and fuel cell generate both electricity and heat, their power outputs are calculated using electricity efficiency (η_d^{E}) and heat efficiency (η_d^{T}), given by (10) and (11). The sum of output electric and heating power must always be less than input power after losses are taken into account. Please note that in the implementation, only the input variables are defined. When the output variable is needed in the equation it is instead expressed through the input variable and efficiency as shown in the previous equation. This approach reduces the total number of variables in the model.

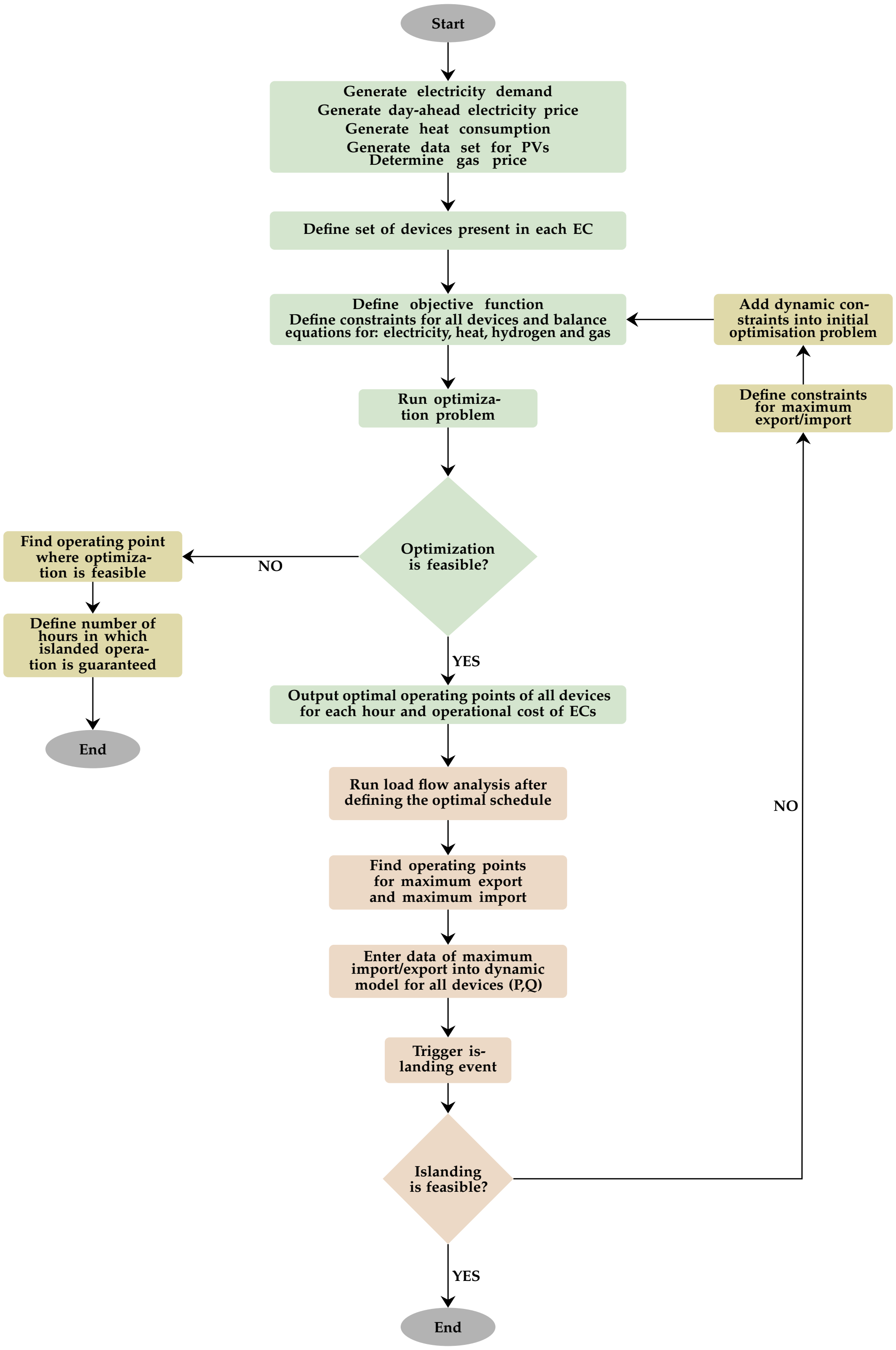

Figure 2. The framework of proposed model: 1st stage in green, 2nd stage in orange, 3rd stage in yellow.

$$\overline{P}_d^{\min} x_{d,m,t} \leq \overline{p}_{d,m,t} \leq \overline{P}_d^{\max} x_{d,m,t} \forall t, m, d \in \mathcal{D}_m^C \tag{2}$$

$$\overline{p}_{d,m,t} \leq \overline{P}_d^{\max} x_{d,m,t}^{\mathrm{c}} \forall t, m, d \in \mathcal{D}_m^S \tag{3}$$

$$\underline{p}_{d,m,t} \leq \underline{P}_d^{\max} x_{d,m,t}^{\mathrm{d}} \forall t, m, d \in \mathcal{D}_m^S \tag{4}$$

$$x_{d,m,t}^{\mathrm{c}} + x_{d,m,t}^{\mathrm{d}} \leq 1 \forall t, m, d \in \mathcal{D}_m^S \tag{5}$$

$$e_{d,m,t} = e_{d,m,t-1} + \overline{p}_{d,m,t} \eta_d^{\mathrm{c}} - \underline{p}_{d,m,t} \frac{1}{\eta_d^{\mathrm{d}}} \forall t, m, d \in \mathcal{D}_m^S \tag{6}$$

$$E_d^{\min} \leq e_{d,m,t} \leq E_d^{\max} \forall t, m, d \in \mathcal{D}_m^S \tag{7}$$

$$x_{d,m,t} - x_{d,m,t-1} \leq z_{d,m,t} \qquad \begin{array}{l} \forall t, m \\ \forall d \in \mathcal{D}_{b,m} \cup \mathcal{D}_{c,m} \end{array} \tag{8}$$

$$\underline{p}_{d,m,t} = \eta_d \overline{p}_{d,m,t} \begin{array}{l} \forall t, m \\ \forall d \in \mathcal{D}_{b,m} \cup \mathcal{D}_{e,m} \cup \\ \mathcal{D}_{h,m} \end{array} \tag{9}$$

$$\underline{p}_{d,m,t}^{\mathrm{E}} = \eta_d^{\mathrm{E}} \overline{p}_{d,m,t} \begin{array}{l} \forall t, m \\ \forall d \in \mathcal{D}_{c,m} \cup \mathcal{D}_{f,m} \end{array} \tag{10}$$

$$\underline{p}_{d,m,t}^{\mathrm{T}} = \eta_d^{\mathrm{T}} \overline{p}_{d,m,t} \begin{array}{l} \forall t, m \\ \forall d \in \mathcal{D}_{c,m} \cup \mathcal{D}_{f,m} \end{array} \tag{11}$$

Each EC is based on a specific energy vector: electricity, gas, and hydrogen. Therefore, the energy balancing equations for each energy vector of the considered EC are written to represent interconnections between devices along with the balancing equation for heat energy. Heat, electricity, hydrogen, and gas balances are given by Equations (12)–(15), respectively. Heat balance Equation (12) ensures that there is enough local heat production to satisfy the load. Electricity balance Equation (13) adds up all consumption and production of electricity while it can sell surpluses or buy deficits from the market. The produced hydrogen has to be stored or consumed since it cannot be bought or sold on any market (14) (acquired from an outside source). Since the gas is bought in a single bid for a 24 h period on the day-ahead market, its consumption must be summed for the entire optimization horizon (15).

$$\sum_{n \in \mathcal{N}_m} L_{n,m,t}^{\mathrm{T}} = \sum_{d \in \mathcal{D}_{b,m} \cup \mathcal{D}_{h,m}} \underline{p}_{d,m,t}^{\mathrm{T}} + \sum_{d \in \mathcal{D}_{c,m} \cup \mathcal{D}_{f,m}} \underline{p}_{d,m,t}^{\mathrm{T}} + \sum_{d \in \mathcal{D}_{\tau,m}} \left(\underline{p}_{d,m,t}^{\mathrm{T}} - \overline{p}_{d,m,t}^{\mathrm{T}} \right) \tag{12}$$

$$\begin{aligned} \textstyle\sum_{n \in \mathcal{N}_m} L_{n,m,t}^{\mathrm{E}} = \textstyle\sum_{n \in \mathcal{N}_m} PV_{n,m,t}^{\mathrm{E}} + \overline{\epsilon}_{m,t} - \underline{\epsilon}_{m,t} - \textstyle\sum_{d \in \mathcal{D}_{e,m} \cup \mathcal{D}_{h,m}} \overline{p}_{d,m,t}^{\mathrm{E}} \\ + \textstyle\sum_{d \in \mathcal{D}_{c,m} \cup \mathcal{D}_{f,m}} \underline{p}_{d,m,t}^{\mathrm{E}} + \textstyle\sum_{d \in \mathcal{D}_{\beta,m}} \left(\underline{p}_{d,m,t}^{\mathrm{E}} - \overline{p}_{d,m,t}^{\mathrm{E}} \right) \end{aligned} \tag{13}$$

$$0 = \sum_{d \in \mathcal{D}_{e,m}} \underline{p}_{d,m,t}^{\mathrm{H}} - \sum_{d \in \mathcal{D}_{f,m}} \overline{p}_{d,m,t}^{\mathrm{H}} + \sum_{d \in \mathcal{D}_{\hbar,m}} \left(\underline{p}_{d,m,t}^{\mathrm{H}} - \overline{p}_{d,m,t}^{\mathrm{H}} \right) \tag{14}$$

$$\gamma_m = \sum_{t \in \mathcal{T}} \left(\sum_{d \in \mathcal{D}_{c,m}} \overline{p}_{d,m,t}^{\mathrm{G}} + \sum_{d \in \mathcal{D}_{b,m}} \overline{p}_{d,m,t}^{\mathrm{G}} \right) \tag{15}$$

2.2. Dynamic Model

In this section, dynamic models of devices in each EC are described. The electrical models of ECs and devices with corresponding control systems are modeled in DIgSILENT PowerFactory 2019.

The network model is based on a real three-phase low-voltage distribution feeder of Zagreb, Croatia. Residential loads are modeled as constant impedance loads. CIG takes full advantage of available grid-forming schemes as RES should provide voltage and frequency references during islanded operation of EC. Since the grid-forming capability depends on the available energy on the DC side, appropriate control schemes are chosen for each device; CIG with a sufficient amount of energy at the DC side (FC, BESS) is controlled as PQ-VSM, while sources with a negligible amount of energy (PV) are controlled as DCVQ-VSM. VSM technologies emulate the static and dynamic performance of synchronous machines, i.e., their inertia and damping effect. Therefore, their implementation is based on some form of the swing equation, assuming the presence of the virtual rotor and virtual governor. Converter-interfaced loads (electrolyzer) are grid-following operating in grid-supporting mode, which means they can adjust their output active and reactive power according to frequency and voltage changes, respectively. All grid-side converters are voltage source converters (VSCs). The design of inner voltage and current control loops is not described in detail, for which we refer the reader to [34].

2.2.1. Electrolyzer

The electrolyzer is a responsive, flexible end-use load [35] that uses electric power to produce hydrogen and can participate in the procurement of ancillary services, such as frequency balancing, voltage control, and congestion management [36]. The electrolyzer is based on the polymer electrolyte membrane (PEM) technology that is promising for large-scale applications. Compared to the other types of electrolyzers (e.g., alkaline electrolyzers, anion exchange membrane electrolyzers, and solid oxide electrolyzers), PEM electrolyzers have a host of advantages, such as lowest capital cost [37], higher power density, scalable design, wider dynamic range [38], wide partial load range, and high adaptability in terms of operation [39]. In this paper, the electrolyzer is modeled as grid-following converter-interfaced load, as shown in Figure 3.

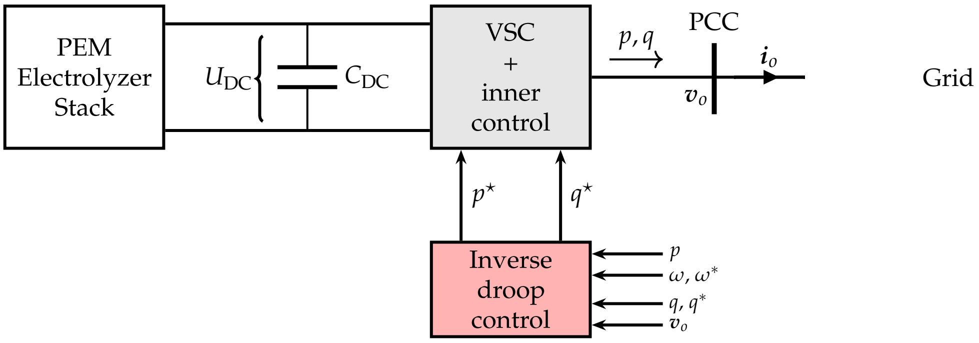

Figure 3. Dynamic model of PEM electrolyser system: PEM Electrolyzer Stack [40–42], Inverse droop control [43,44].

The electrolyzer model consists of three sub-models: electrical, thermal, and H_2 production sub-model [40,41]. The H_2 production sub-model can be ignored since it does not provide any signals to the other two sub-models. Since the thermal constant of the electrolyzer is in the order of hours, but the simulation time-horizon of interest is several seconds, the thermal sub-model is not necessary [40]. In other words, the temperature of the electrolysis stack can be assumed to be constant during dynamic analysis. Therefore, the electrical sub-model is a sufficiently accurate representation of the electrolyzer in dynamic analysis. The electrolyzer stack model is implemented according to [40–42]. The equivalent electrical circuit of the electrolyzer is given by a voltage source in series with internal resistance and an electrical double layer (EDL) branch [41,42]. The magnitude of the voltage source is given by Nernst Equation (16):

$$E = E_0 - 0.85 \times 10^{-3}(T - 298.15) + \frac{RT}{zF} \ln\left(\frac{p_{H_2} p_{O_2}^{0.5}}{p_{H_2O}}\right) \tag{16}$$

where E_0 is the constant reversible voltage, R is the universal gas constant, F is the Faraday constant, z is the number of electrons in reaction ($z = 2$ for hydrogen–oxygen reaction), T is the stack temperature, p_{H_2} is hydrogen partial pressure, p_{O_2} is oxygen partial pressure, and p_{H_2O} is water vapor pressure. Because of the ideal gas law ($pV = nRT$), the pressure is also considered constant. The output voltage of electrolysis cell V_{cell} is the result of reversible voltage, ohmic voltage drop, and voltage drop on the EDL branch V_{EDL}. Ohmic voltage drop is a function of membrane resistance R_{ohm}, which is assumed to be constant, and the current density i.

$$V_{\text{cell}} = E + V_{\text{EDL}} + R_{\text{ohm}} \cdot i \tag{17}$$

The EDL voltage drop is given by (18):

$$\frac{dV_{\text{EDL}}}{dt} = \frac{i}{C_{\text{EDL}}} - \frac{V_{\text{EDL}}}{R_a C_{\text{EDL}}} \tag{18}$$

where R_a is the double-layer resistance associated with activation voltage drop and C_{EDL} is the double-layer capacitance related to concentration voltage drop. The electrolyzer stack voltage V_{st} is then calculated by (19) where N is the number of electrolysis cells in the stack.

$$V_{\text{st}} = N \cdot V_{\text{cell}} \tag{19}$$

The current density is initialized and calculated as a function of electrolyzer input power P, stack voltage V_{st}, and cell area A_{cell} in cm^2 (20).

$$i = \frac{P}{V_{\text{st}} A_{\text{cell}}} \tag{20}$$

Technically, electrolyzers are capable of providing fast frequency response with the presence of an accurate control system. They respond to over-frequency conditions by increasing their power/current, and to under-frequency conditions by reducing their power consumption [40]. The following text describes the electrolyzer control system. The reference active power signal $p^\star$ is a result of inverse droop control [43,44], as given by expression (21):

$$p^\star = p + \frac{1}{R}(\omega - \omega^*) \tag{21}$$

where p is the measured input power of the electrolyzer, R is the frequency droop, ω is the measured grid frequency (PLL) at the PCC, and ω^* is the frequency reference.

Moreover, reactive power control is realized as follows:

$$q^\star = \frac{1}{\|v_o\|}\left(K_{pq} + \frac{K_{iq}}{s}\right)(q^* - q) \tag{22}$$

where $\|v_o\|$ is the magnitude of terminal voltage, K_{pq} and K_{iq} are PI controller gains, q^* is the reference reactive power ($q^* = 0$ in this paper), and q is the measured reactive power of the electrolyzer system [38]. Active and reactive power references $(p^\star, q^\star)$ are inputs to the inner voltage and current control loops [34].

2.2.2. Fuel Cell

The fuel cell is based on the PEM technology that converts the chemical energy of hydrogen and oxygen or air into electrical energy and thermal energy [45]. It consists of two electrodes, anode and cathode, separated by a polymer electrolyte [46,47]. Each of these components is assumed as a one-dimensional system [48]. At the anode, the hydrogen supplied from an external tank is dissociated into protons as described by (23). Hydrogen ions are transferred to the cathode via osmosis as the polymer electrolyte permits the transfer of only positive ions, while an external electric circuit is used to link electrodes and to carry electrons, producing DC electricity. At the cathode, the oxidant is merged with electrons and hydrogen ions as described by (24). The total chemical reaction occurring in the fuel cell is shown by (25), resulting in water, residual heat, and electricity [45,49–51]. Thermal energy is associated with atomic and molecular vibration [52].

$$\mathrm{H_2} \longrightarrow 2\,\mathrm{H^+} + 2\,\mathrm{e^-} \tag{23}$$

$$2\,\mathrm{H^+} + 2\,\mathrm{e^-} + \frac{1}{2}\,\mathrm{O_2} \longrightarrow \mathrm{H_2O} \tag{24}$$

$$\mathrm{H_2} + \frac{1}{2}\,\mathrm{O_2} \longrightarrow \mathrm{H_2O} + \text{heat} + \text{electricity} \tag{25}$$

The PEM fuel cell behavior is non-linear and dependent on different factors, such as temperature, reactant pressure, membrane hydration, and reactant concentrations [53]. However, the following assumptions are considered for dynamic analysis:

- Due to slow thermal dynamics of the fuel cell, the temperature is assumed to be constant, i.e., it can be well-controlled by the cooling system [54].
- The gases are ideal and uniformly distributed [55].
- Because of slow changes in the humidifier, the input humidity is constant [54].
- The internal resistance is constant [56].
- The output stack voltage is described by the Nerst equation [56].

The fuel cell and the electrolyzer have the same electrochemical model. Therefore, the same equivalent electrical circuit is used to represent the fuel cell [57]. However, the current flow is in the opposite direction since the fuel cell produces electricity, while the electrolyzer uses electricity to produce hydrogen. All equations that describe the electrolyzer model are also valid for the fuel cell model, except that the fuel cell voltage is now described as (26) due to the opposite current direction.

$$V_{\text{cell}} = E - V_{\text{EDL}} - R_{\text{ohm}} \cdot i \tag{26}$$

The described fuel cell dynamics are subsumed under the PEM fuel cell stack in Figure 4. However, the challenging part is its control system that is implemented as PQ-VSM, i.e., the active and reactive power outputs are controlled. The implementation of the active power controller is based on the swing Equations (27) and (28), representing the dependence of the virtual rotor speed and power balance:

$$\frac{d\omega^{\star}_{\text{VSM}}}{dt} = \frac{1}{T_a}\left(p^* - p - K_d(\omega^{\star}_{\text{VSM}} - \omega) - K_\omega(\omega^{\star}_{\text{VSM}} - \omega^*)\right) \tag{27}$$

$$\frac{d\theta^{\star}_{\text{VSM}}}{dt} = 2\pi f_n \omega^{\star}_{\text{VSM}} \tag{28}$$

where p^* is the active power reference, p is the measured electrical power flowing from the fuel cell system, and T_a is the mechanical time constant that corresponds to $2H$ in conventional synchronous machines. Terms $K_d(\omega^{\star}_{\text{VSM}} - \omega)$ and $K_\omega(\omega^{\star}_{\text{VSM}} - \omega^*)$ model the damping and droop control, respectively, in which $\omega^{\star}_{\text{VSM}}$, ω and ω^* are respective VSM speed, estimated grid frequency (PLL), and grid frequency reference. $\theta^{\star}_{\text{VSM}}$ is the internal converter angle reference, with f_n being the nominal frequency in Hz. Since the PQ-VSM has the ability to provide the inertial response and damping effect, as well as the power–frequency droop control, the fuel cell controlled in this way will change its output power according to the frequency deviations.

The reactive power control of the fuel cell system is based on the Q/V (reactive power/voltage) droop strategy (29):

$$v^\star = v^* + K_q(q^* - q) \tag{29}$$

where v^* is the external voltage amplitude reference, q^* is the reactive power reference, q is the measured reactive power, and K_q is the reactive power droop gain.

Voltage and angle references $(v^\star, \theta^\star_{\text{VSM}})$ provided by these controllers are input signals to the cascaded inner control loops. Detailed implementation of the VSM converter is explained in [58].

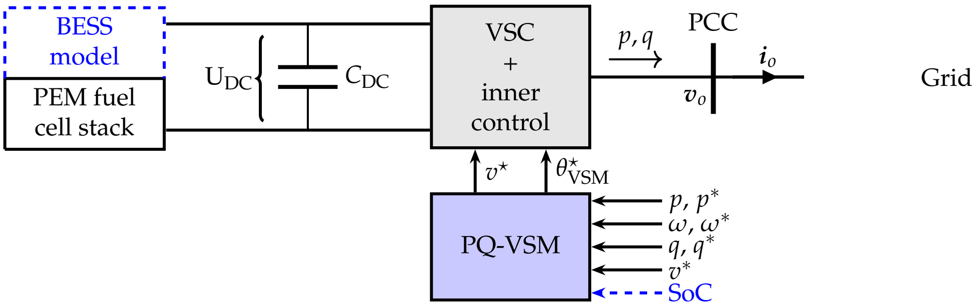

Figure 4. Dynamic model of a fuel cell system and battery system (in blue): BESS model [59], PEM fuel cell stack [57], PQ-VSM [58].

2.2.3. Battery Energy Storage System

The BESS model consists of a DC-side model, battery cell model, and control system. The DC side serves to detect the DC voltage U_{DC} (30) and calculate the DC current (31) that is needed as the input signal to the battery cell model. The active power signal P is obtained by load flow analysis and measured in MW, while DC current I is expressed in kiloamperes (kA).

$$\frac{dU_{\text{DC}}}{dt} = \frac{V_{\text{term}} - U_{\text{DC}}}{0.01} \tag{30}$$

$$I = \frac{P \cdot 10^3}{U_{\text{DC}}} \tag{31}$$

The battery cell model is based on the available model in the PowerFactory library and can be found in [59]. The battery model is described by Equations (32)–(35):

$$I_{\text{cell}} = \frac{I}{N_p} \tag{32}$$

$$\text{SoC} = -\frac{1}{3600C_r}\int_{t_0}^{t} I_{\text{cell}}(\tau)d\tau \tag{33}$$

$$U_{\text{cell}} = U_{\max} \cdot \text{SoC} + U_{\min} \cdot (1 - \text{SoC}) - I_{\text{cell}} \cdot R_{\text{icell}} \tag{34}$$

$$V_{\text{term}} = U_{\text{cell}} \cdot N_s \tag{35}$$

where N_s is the amount of serial connected cells; N_p is the amount of parallel connected cells; C_r is the rated cell capacity in Ah; $U_{\max}$ and $U_{\min}$ are the maximum and minimum allowed voltages of a battery cell; R_{icell} is the internal resistance per cell [59]. Output signals are the current of single cell I_{cell}, state-of-charge SoC, and battery terminal voltage V_{term}. Furthermore, the BESS control system is also based on the PQ-VSM, as shown in Figure 4. Therefore, the active and reactive power controllers are implemented in the same way as for the fuel cell control system. Additionally, the BESS control system includes charge control that checks whether the current and state-of-charge (SoC) values are within certain limits. It prevents discharging of the battery if SoC falls below the minimum threshold, and prevents charging of the battery if SoC is above the maximum threshold. The device-side model is subsumed under the BESS block in Figure 4. The BESS and its control system are described in detail in [58,60].

2.2.4. Photovoltaic Unit

The PV dynamic model is presented in Figure 5 where the device-side model is subsumed under the PV array. It is also based on the available model in PowerFactory and described by (36)–(39) [61]:

$$U^{\mathrm{mpp}} = N_s k^{T,U} U_0^{\mathrm{mpp}} \frac{\ln E}{\ln E_0} \tag{36}$$

$$I_{PV} = N_p k^{T,I} I_0^{\mathrm{sc}} \frac{E}{E_0} \left[1 - e^{\frac{N_s^{-1} U_{\mathrm{DC}} - U^{\mathrm{oc}}}{N_s^{-1} U^{\mathrm{mpp}} - U^{\mathrm{oc}}} \ln\left(1 - \frac{I_0^{\mathrm{mpp}}}{I_0^{\mathrm{sc}}}\right)} \right] \tag{37}$$

$$U^{\mathrm{oc}} = k^{T,U} U_0^{\mathrm{oc}} \frac{\ln E}{\ln E_0} \tag{38}$$

$$P_{\mathrm{PV}} = U \cdot I_{\mathrm{PV}} \tag{39}$$

where N_s is a number of modules in series that form a string; N_p is the number of strings in parallel that form an array; U_0^{mpp} and I_0^{mpp} are maximum power point voltage and current; U_0^{oc} and I_0^{sc} are open-circuit voltage and short-circuit current; $k^{T,U}$ and $k^{T,I}$ are linear temperature correction factors for voltage and current [61]. The PV voltages and currents are assumed at standard conditions: $E_0 = 1000\ Wm^{-2}$ and $T = 25\ ^{\circ}\mathrm{C}$. Outputs of PV array model are the maximum power point voltage U^{mpp} and active power P_{PV}.

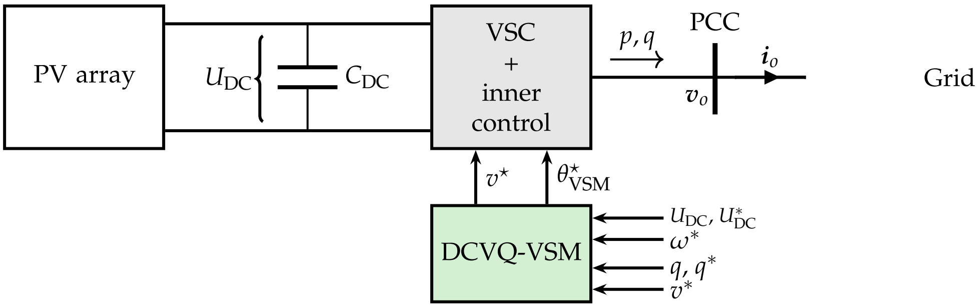

Figure 5. Dynamic model of rooftop PV system: PV array [61], DCVQ-VSM [58,62].

The PV system (Figure 5) is operated in MPPT mode, so the control system of the PV converter is based on the DCVQ-VSM where the DC link voltage and reactive power are controlled. The reactive power control is achieved by setting the reference values (q^*,v^*) as in PQ-VSM. The DC-link voltage controller provides the frequency reference value and achieves active power synchronization utilizing the dynamics of the DC-link capacitor to achieve the inertial response (albeit small due to the negligible amount of stored energy in the PV system). The DC-link voltage is a function of power flow through the DC-link capacitor and its capacity C_{DC} as given by (40):

$$C_{\mathrm{DC}} \frac{dU_{\mathrm{DC}}}{dt} = \frac{1}{U_{\mathrm{DC}}} \Big(p_{\mathrm{PV}} - p \Big) \tag{40}$$

where p_{PV} is the per-unit value of PV active power, while p is the per-unit value of converter power output. VSM speed $\omega^\star_{\mathrm{VSM}}$ is governed by (41):

$$\omega_{\mathrm{VSM}}^{\star} = \omega^{*} + \frac{s + K_T}{K_J s + K_D}[(U_{\mathrm{DC}})^2 - (U_{\mathrm{DC}}^{*})^2] \tag{41}$$

where ω^* is the grid frequency reference; U_{DC} is the measured DC-link voltage; $\mathrm{U}_{\mathrm{DC}}^{*}$ is the reference value of the DC-link voltage; K_T is the DC-link voltage tracking coefficient; K_D is the damping coefficient; K_J is the inertia emulation coefficient [62]. The internal converter angle is the same as in (28). This control strategy enables the provision of inertial response and damping effect, yet the power–frequency droop control cannot be achieved, and therefore the PV unit cannot contribute to the steady-state frequency value. The detailed model of the implemented PV system can be found in [58].

2.2.5. CHP Unit and Heat Pump

The CHP unit in the GEC is modeled as a synchronous (diesel) generator with a $GAST$ gas turbine-governor model and $AC5A$ excitation system, both with default parameters in PowerFactory.

The heat pump (HP) in EEC is modeled as an induction motor with a single cage rotor. HP is directly connected to the grid. Its mechanical torque is quadratically proportional to the motor speed.

2.2.6. on the Controller Parameters

In previous subsections, implementations of active and reactive power controllers for different devices are discussed. Although these are different control strategies, similar requirements are set to adjust their parameters as improper tuning may lead to instability in some cases.

Therefore, the following paragraphs aim to explain the parameter tuning of active power controllers. Regardless of the control strategy (PQ-VSM, DCVQ-VSM, droop control), the inertia constant should be tuned according to the desired sensitivity to grid-side power imbalance, and typical values are [1, 20] s [63].

Droop gains can be determined according to maximum power rating and maximum allowable frequency deviations. The standard range is [10, 100] p.u. The higher the droop constant, the smaller the frequency steady-state deviation [63,64].

Furthermore, the damping coefficient of virtual inertia-based control strategies has a wide range, i.e., [0, 1000] p.u. However, too large a value can increase oscillations [63,64].

Similar to frequency droop gain, the reactive power droop gain can be determined by the maximum power rating and maximum allowable voltage deviations, resulting in the usual range of [0, 0.2] p.u.

Since all grid-side converters are modeled as a VSC, the method of the parameter tuning of cascaded voltage and current loops should be mentioned. In this paper, their parameters are tuned by a trial-and-error process. Nonetheless, it should be taken into account that the outer control loop (voltage controller) must be slower (by about 5–10 times or more) than the inner control loop (current controller) to achieve timescale separation.

3. Case Study

The presented EC layouts (Figure 1) are chosen to showcase a set of diverse ECs based on different energy vectors that developed organically over time, as opposed to MGs, which are generally sized and built from scratch as standalone systems in the existing literature. In this sense, organic development implies that the existing end-users in the LV network have decided to incorporate different technology vectors over a certain period of time and form an EC. Note that because of the limited space and a large number of network elements, a detailed list of parameters was omitted. Most relevant case study information is provided below.

All ECs contain rooftop PVs for electricity production. Each EC consists of 30 households ($|\mathcal{N}_m| = 30$) with a 5 kW rooftop PV system. Each EC was given a different energy storage that logically fits in. Fully electrified EC has a BESS at every household

($|\mathcal{D}_{\beta,\mathrm{EEC}}| = 30$), sized so that it can store all electricity from PV in one hour while the heat demand is covered by a central HP ($|\mathcal{D}_{h,\mathrm{EEC}}| = 1$). Gas-based EC has a central heat storage ($|\mathcal{D}_{\tau,\mathrm{GEC}}| = 1$) since it is based on a central CHP system ($|\mathcal{D}_{c,\mathrm{GEC}}| = 1$) whose production is mainly driven by heat consumption. It can store one hour worth of heat produced from the CHP. Similarly, hydrogen-based EC has a central hydrogen storage ($|\mathcal{D}_{\hbar,\mathrm{HEC}}| = 1$) that can store one hour of hydrogen production from a central electrolyzer ($|\mathcal{D}_{e,\mathrm{GEC}}| = 1$). A central FC system ($|\mathcal{D}_{f,\mathrm{GEC}}| = 1$) is used to generate heat alongside electricity. HP, CHP, and FC are sized so that they can cover all the heat consumption that may occur. Therefore, sizing the electrical output of HPs, CHPs, and FCs was secondary. In hydrogen-based EC, the electrolyzer was sized so that it can produce enough hydrogen in order for the fuel cell to operate for 1 h. For more details on device sizing, we refer the reader to [65].

Device parameters are given in Table 2. Electricity demand is generated using *LoadProfileGenerator 8.9.0.0.* software [66]. Scenarios of PV production are generated using [67] with the weather set for Zagreb, Croatia. Electricity prices are taken from Croatian power exchange (CROPEX) [68]. The heat consumption set is generated from [69] and resembles the climate conditions in Croatia. It is assumed that the gas price has a singular value of $\pi^{\mathrm{G}} = 85.7$ €/MWh taken from Central European Gas Hub Virtual Trading Point [70].

Table 2. Parameters of all devices considered by ECs.

Device	Power Rating	Efficiency	Capacity
Heat pump	$\overline{P}_h^{\max} = 120$ kW	$\eta_h = 2.5$	-
CHP	$\overline{P}_c^{\max} = 430$ kW	$\eta_c^{\mathrm{E}} = 0.22$ $\eta_c^{\mathrm{T}} = 0.7$	-
Boiler	$\overline{P}_b^{\max} = 180$ kW	$\eta_b = 0.85$	-
Fuel cell	$\overline{P}_f^{\max} = 580$ kW	$\eta_f^{\mathrm{E}} = 0.37$ $\eta_f^{\mathrm{T}} = 0.52$	-
Electrolyzer	$\overline{P}_e^{\max} = 880$ kW	$\eta_e = 0.66$	-
Battery (1 per household)	$\overline{P}_\beta^{\max} = 5$ kW $\underline{P}_\beta^{\max} = 5$ kW	$\eta_\beta^{\mathrm{c}} = 0.9$ $\eta_\beta^{\mathrm{d}} = 0.9$	5 kWh
Heat storage	$\overline{P}_\tau^{\max} = 335$ kW $\underline{P}_\tau^{\max} = 335$ kW	$\eta_\tau^{\mathrm{c}} = 0.9$ $\eta_\tau^{\mathrm{d}} = 0.9$	335 kWh
Hydrogen storage	$\overline{P}_\hbar^{\max} = 600$ kW $\underline{P}_\hbar^{\max} = 600$ kW	$\eta_\hbar^{\mathrm{c}} = 1$ $\eta_\hbar^{\mathrm{d}} = 1$	600 kWh

In the optimization model (1)–(15), the power flow equations were omitted for two reasons: (i) for simplicity; (ii) we assume that in normal, on-grid operation, the DSO is in charge of voltage and power flow control. This is a realistic assumption since EC is a part of an existing distribution system, and for every existing end-user grid connection, an adequate grid integration study must have been conducted a priori by the DSO. Additionally, in case there are some interruptions of electricity supply in the rest of the grid, ECs are also allowed (by the DSO) to transition into islanding operation. During islanded operation, the EC manager is in charge of the grid control until it resynchronizes to the main grid. Therefore, power flow is run in the second stage to check if the node voltages and line loadings are within predefined bounds.

The network model of each EC (Figure 1) is identical; short-circuit voltage of the 10/0.42 kV transformer is 4%. The main line from the feeder consists of 1 kV 4 × 240 PP41-A cable segment with $R = 0.136\ \Omega/\mathrm{km}$, $L = 0.252$ mH/km, and 1 kV 4 × 240 mm^2 NYBY cable segment with $R = 0.0787\ \Omega/\mathrm{km}$, $L = 0.23$ mH/km. The total length of the feeder line is about 600 m. The line connecting each household to the main line is a 1 kV 3 × 35 mm^2 NFA2X cable with $R = 0.868\ \Omega/\mathrm{km}$ and $L = 0.264$ mH/km, with length in the range 5–25 m.

4. Simulations and Results

4.1. Stage 1: Initial Optimization

The optimization is executed for one year with steps of one hour, i.e., in total, there are 8760 steps ($|\mathcal{T}| = 8760$). The operational cost and operating point of all devices for each hour are calculated by the optimization model for all ECs. In this paper, the results focus on maximum export and maximum import at the PCC as these are the points of the largest active power mismatch. Thus, they are the main driver of transient dynamics during islanding.

4.1.1. Fully Electrified EC

The annual operational cost of the fully electrified EC is EUR 7966. Figure 6 shows electricity exchange with the market for the whole year on an hourly basis. During the winter period when heating consumption is high and PV production is generally lower, EC buys large amounts of electricity. On the contrary, during summer months, there is no heating production and PV production is higher, and thus EC mostly sells electricity. The case of maximum export happened in hour 5267 when all PV units generate 4.2 kW and all BESSs are discharged with 4.5 kW. There is no HP consumption, and the total load is 2.3 kW. This leads to a total export of 257.7 kW. In the case of the maximum import, there is no PV production and all BESSs are charged with 5.0 kW. The HP consumption amounts to 94.9 kW, while the total load is 1.4 kW. This leads to the total import of 246.3 kW in hour 796.

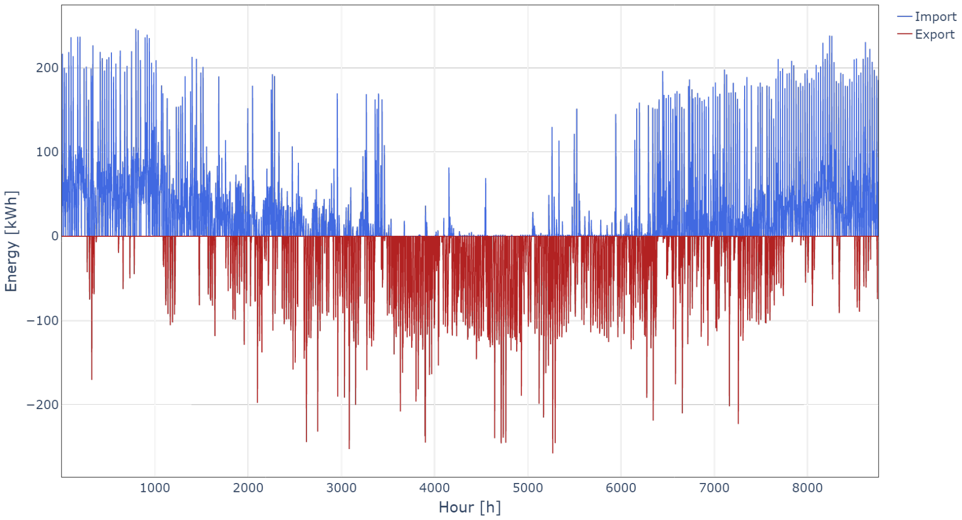

Figure 6. Electricity exchange of fully electrified EC.

4.1.2. Gas-Based EC

The result of the gas-based EC annual operational cost is EUR 24,420. Figure 7 shows electricity exchange with the market for the whole year on an hourly basis. EC based on gas technologies has a mostly similar pattern through the whole year because their heating system is not powered by electricity. Overall, less electricity is needed, being replaced with 580 MWh of gas. This EC mostly exports electricity produced from PV on the market, importing only during insufficient production. During the maximum export, the CHP unit and all PV units generate 94.6 kW and 3.7 kW, respectively, while the total load is 4.6 kW. The maximum export happened in hour 7162 and amounts to 200.2 kW. The case of the maximum import happened in hour 4069 when there is no production of the CHP unit and all PV units generate only 0.5 kW. The total load is 136.9 kW. This leads to the maximum import of 121.9 kW.

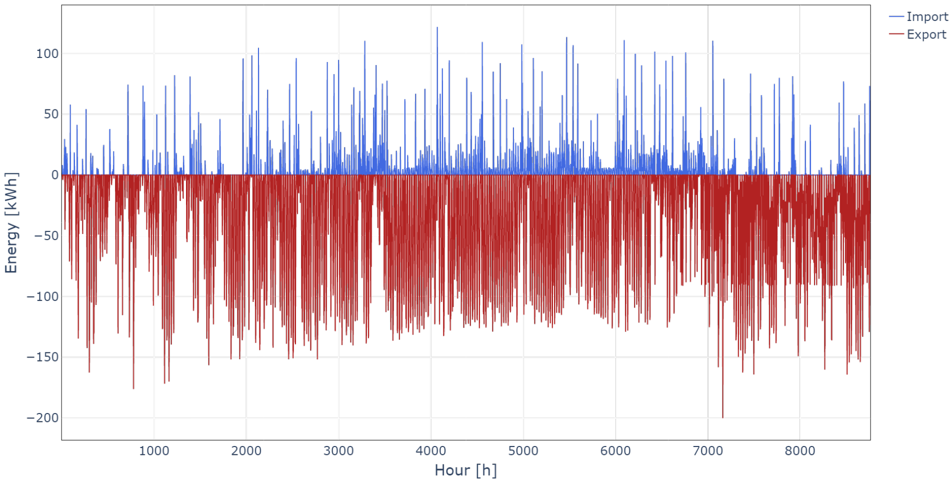

Figure 7. Electricity exchange of gas-based EC.

4.1.3. Hydrogen-Based EC

The annual operational cost of hydrogen-based EC is EUR 97196. Figure 8 presents electricity import/export for hydrogen-based EC for the whole optimization horizon. This EC is the most electricity-intensive, because of the lower efficiency of hydrogen heating. This is concluded from high electricity import during the heating period and exporting excess PV production only during the non-heating period. During the maximum export (hour 323), all PV units generate 4.0 kW and the FC generates 100.0 kW. The total load is 2.1 kW and there is no consumption from the electrolyzer. The maximum export amounts to 219.8 kW. In the second case, maximum import (hour 2561), all PV units generate only 0.2 kW, the FC generates 20.0 kW, while the total load is 57.5 kW and the electrolyzer consumes 880.0 kW. This results in a maximum import of 912.5 kW.

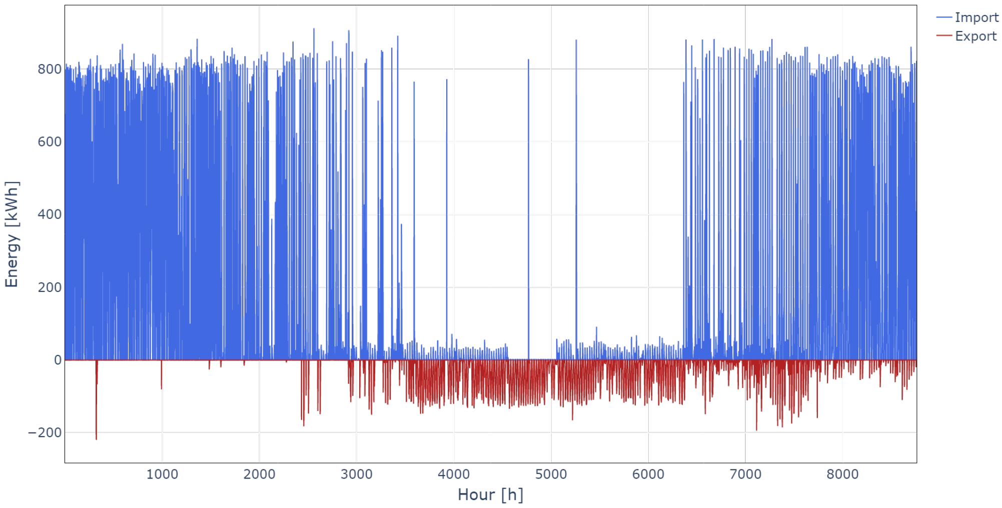

Figure 8. Electricity exchange of hydrogen-based EC

4.2. Stage 2: Dynamic Analysis

The dynamic stability of ECs is verified for two extreme operating points obtained by the optimization in the first stage, e.g., maximum export/import to/from the electric grid since these are the most challenging points for ECs to maintain the stability in case of islanding. The goal is to check the ability of all three ECs to achieve a stable transition to islanded operation. The stable transition is defined by reaching the steady state and satisfying frequency and voltage constraints after islanding, i.e., terminal voltages have to remain within ±10% of nominal value, the maximum permissible frequency deviation is limited to ±2 Hz in the first second after islanding, after which the limit is set to ±1 Hz, and RoCoF is limited to ±2 Hz/s measured over a 500 ms time window. Firstly, the load flow analysis is executed to calculate the steady-state performance and to initialize dynamic models. Then, the RMS simulation is performed with the defined islanding event at time $t = 4$ s, i.e., the switch event of the external grid is performed at $t = 4$ s. The results of the dynamic analysis for all ECs are presented below.

4.2.1. Fully Electrified EC

Although no synchronous generation is present, the EEC can achieve a stable transition to the islanded mode for both operating points as their control systems are based on grid-forming converters with virtual inertia. During the transition to islanded mode in the maximum export scenario, PV units temporarily change their output power, while BESS switches to charge mode to store a surplus of the generation power (Figure 9d). The frequency stabilizes at the above-nominal value after re-establishing the power balance (Figure 9a). RoCoF and terminal voltage constraints are satisfied as shown in Figure 9b,c, respectively. During the transition to islanded mode in a maximum import scenario, BESSs are charged with maximum power and there is no PV production. The islanding is feasible in this case as well, as frequency, RoCoF, and voltage constraints are satisfied (Figure 10a–c). BESS switches to discharge mode after islanding to establish the power balance (Figure 10d).

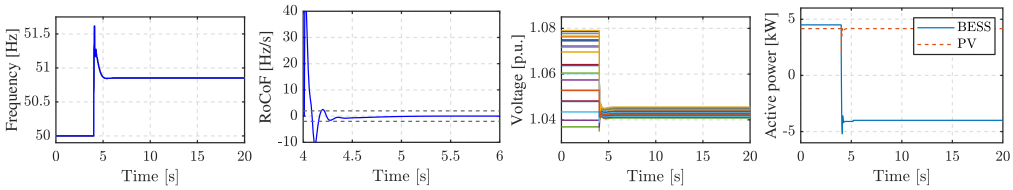

(a) **(b)** **(c)** **(d)**

Figure 9. Results of EEC for maximum export: (**a**) Frequency, (**b**) RoCoF, (**c**) Terminal voltages, (**d**) BESS and PV active power response.

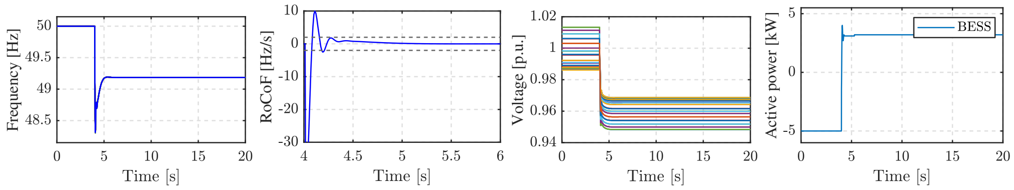

(a) **(b)** **(c)** **(d)**

Figure 10. Results of EEC for maximum import: (**a**) Frequency, (**b**) RoCoF, (**c**) Terminal voltages, (**d**) BESS active power response.

4.2.2. Gas-Based EC

The islanding of GEC is infeasible for the case of the maximum export since the PV production is larger than the total power consumption, and CHP cannot provide enough of a downward reserve. For these reasons, the frequency and RoCoF increase beyond prescribed limits, as shown in orange in Figure 11a,b, respectively. To achieve stable transition during maximum export, PVs need to be curtailed such that the CHP electrical output is equal to or larger than the export power (i.e., that there is enough of a downward reserve). The frequency, RoCoF, and voltage after PV curtailment are shown in blue in Figure 11a, Figure 11b, and Figure 11c, respectively. The islanding is also infeasible in the case of maximum import. After islanding, the total load is much higher than production and CHP cannot provide enough upward reserve. The frequency and voltage are unstable and constraints are not met, as shown in Figure 12a,c. To achieve the stable transition to islanded operation, the maximum import must be limited to 95 kW. Results with respect to this limit are presented in blue in Figure 12a–c. Note that the infeasibility stems from the fact that GEC was developed organically to satisfy heat and load demand during normal operation; therefore, it does not have the inherent capability to provide islanding services in the worst-case scenario without curtailment or specific investments in CHP sizing or other devices that can provide transient power balancing.

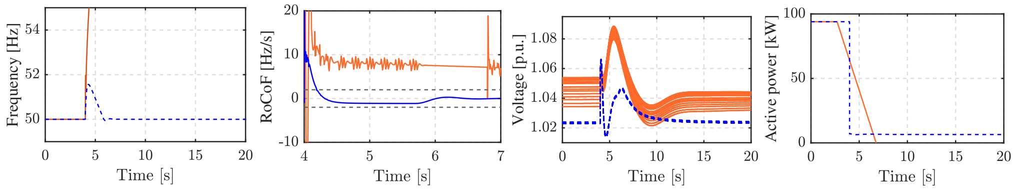

(a) **(b)** **(c)** **(d)**

Figure 11. Results of GEC for maximum export [orange: without constraints, blue: with constraints]: (**a**) Frequency, (**b**) RoCoF, (**c**) Terminal voltages, (**d**) CHP active power.

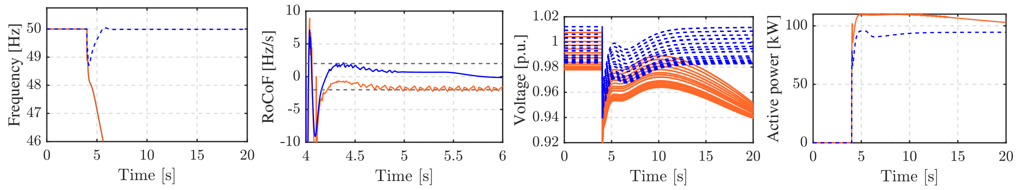

(a) **(b)** **(c)** **(d)**

Figure 12. Results of GEC for maximum import [orange: without constraints, blue: with constraints]: (**a**) Frequency, (**b**) RoCoF, (**c**) Terminal voltages, (**d**) CHP active power.

4.2.3. Hydrogen-Based EC

The HEC is specific due to the presence of a responsive load, the PEM electrolyzer. After islanding during maximum export, the electrolyzer should increase its power consumption. However, the electrolyzer provides the response within 100 ms-1/2 s [41]. With respect to this, the fuel cell has to be able to provide a downward reserve in the first seconds after the disturbance. Since the fuel cell could not provide enough downward reserve until the electrolyzer response, the islanding is infeasible. Results are not shown because the dynamic model could not achieve convergence during the transition. To achieve a stable transition to islanded mode, the maximum export must be limited to 143 kW. Results with constraints are shown in Figure 13. Due to the electrolyzer delay, the islanding in the case of the maximum import is also not achieved. Therefore, the maximum import must be limited to 234 kW. Results with this limitation are shown in Figure 14. Here, the organically sized central hydrogen technologies are also inherently insufficient to provide transient power balancing during the worst-case scenario. Curtailment, artificial sizing of FC-electrolyzer, or investment into specific devices is necessary to achieve stable islanding transition in hydrogen-based EC.

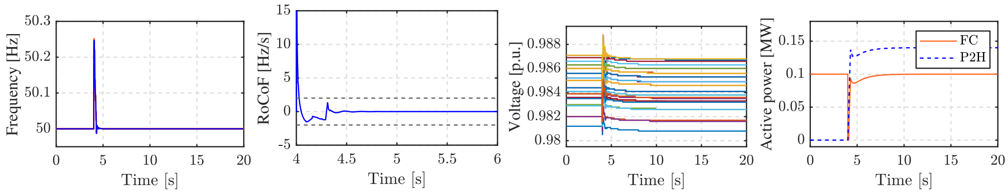

(a) **(b)** **(c)** **(d)**

Figure 13. Results of HEC for maximum export: (**a**) Frequency, (**b**) RoCoF, (**c**) Terminal voltages, (**d**) FC and electrolyzer active power.

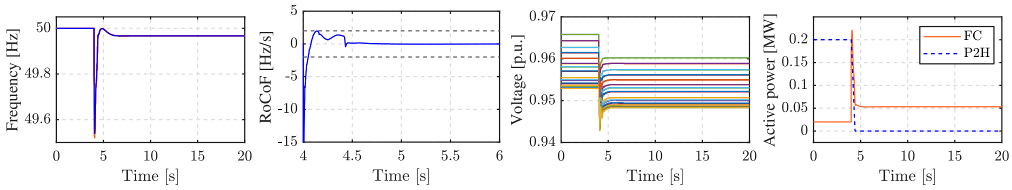

(a) **(b)** **(c)** **(d)**

Figure 14. Results of HEC for maximum import: (**a**) Frequency, (**b**) RoCoF, (**c**) Terminal voltages, (**d**) FC and electrolyzer active power.

4.3. Stage 3: Optimization with Additional Constraints

Constraints obtained from the dynamic analysis in the second stage are incorporated into the initial optimization problem to ensure ECs are always capable of islanding. Since EEC islanding was initially feasible, only GEC and HEC are considered in the third stage.

4.3.1. Gas-Based EC

To achieve the stable off-grid transition of the GEC, two new constraints are added. The maximum import is restricted to 95 kW, while the electrical output of the CHP unit must be equal to or larger than the maximum export. This results in 88.4% higher cost than in the initial problem, i.e., the annual operational cost is EUR 46008.

4.3.2. Hydrogen-Based EC

To ensure the stable off-grid transition of the HEC, the maximum export and maximum import are limited to 143 kW and 234 kW, respectively. However, once the optimization is restarted with these constraints, the model proves infeasible. It can be deduced that the production of hydrogen for heat production is insufficient after adding dynamic constraints. The highest limit that can be set on maximum import for optimization to be feasible is 390 kW, which amounts to an annual operational cost of EUR 103201 (6.2% increase). It is worth mentioning that in normal operation, HEC imports more than 234 kW for 1368 h (15.6% of the year).

4.4. Discussion

The ability to transition to an islanding mode provides added value for ECs. If it is managed correctly, it can guarantee constant security of supply to EC, while being less dependent on the outside grid and interruptions in it. It also gives an additional layer of benefits to existing technologies, making them more interesting as investments for ECs. For system operators, this alleviates the need to cover part of the grid the EC is in during interruption. It can also provide benefits for system operators in congestion management and system frequency regulation, helping to mitigate or avoid interruption for other end-users. Various technologies are tested for their ability to make such transitions. While under certain conditions all technologies can make such a transition, it was shown that some cannot reach a stable state in worst-case scenarios. Additional constraints were added to ensure a stable transition at any given moment and their economic impact was analyzed. ECs themselves would need to decide for the implementation of such technologies and whether there are benefits of having the ability to always transition to island mode. On a case-to-case basis, they would need to make a cost–benefit analysis and opportunity cost of interrupted supply.

5. Conclusions

A three-stage method is proposed in this article for optimal EC scheduling considering dynamic islanding constraints to ensure a stable off-grid transition. The first and third stages are optimization models based on mixed-integer linear programming. The second stage is a dynamic model to define islanding constraints during worst-case conditions. The optimal schedule of EC is determined by the optimization formulation and translated into the dynamic model to verify the islanding capability. In the case of infeasible islanding, the boundary conditions for stable off-grid transition are defined. They are then propagated back to the initial optimization formulation to determine a new optimal schedule with feasible islanding. The proposed method is applied to three different organically developed ECs: fully electrified, gas-based, and hydrogen-based EC. The results indicate that only fully electrified ECs inherently have adequate islanding capabilities without the need for curtailment or additional investments. On the other hand, the islanding of gas and hydrogen-based ECs is inherently infeasible due to the operational limitations of their devices. Incorporating islanding constraints increased the operational cost of gas-based EC by 88.4%, while hydrogen-based EC operation was deemed infeasible due to insufficient heat production.

Author Contributions: Conceptualization and methodology, all authors; Dynamic and optimisation modelling, B.B., M.K. (Matija Kostelac) and M.K. (Matej Krpan); Dynamic simulations, B.B.; Data curation, M.K. (Matija Kostelac); Investigation, B.B.; Validation, B.B. and M.K. (Matija Kostelac); Writing—Original Draft, B.B. and M.K. (Matija Kostelac); Writing—Review and Editing, B.B., M.K. (Matija Kostelac) and M.K. (Matej Krpan); Visualization, B.B. and M.K. (Matej Krpan); Resources, T.C., Supervision, M.K. (Matej Krpan) and T.C., Project administration, T.C. All authors have read and agreed to the published version of the manuscript

Funding: This research received no external funding.

Acknowledgments: This work has been supported by the European Union through the European Regional Development Fund Operational programme Competitiveness and Cohesion 2014–2020 of the Republic of Croatia under Grant KK.01.1.1.07 “Universal Communication and Control System for Industrial Facilities”, and by Croatian Science Foundation (HRZZ). This work has also been supported in part by the FLEXIGRID project from the European Union’s Horizon 2020 research and innovation programme under grant agreement No 864579. This paper reflects the FLEXIGRID consortium view and the European Commission is not responsible for any use that may be made of the information it contains. Employment of Bojana Barać is fully funded by the Croatian Science Foundation within programme DOK-2021-02.

Conflicts of Interest: The authors declare no conflicts of interest.

Abbreviations

The following abbreviations are used in this manuscript:

BESS	Battery energy storage systems
CIG	Converter-interfaced generation
CHP	Combined heat and power
EC	Energy community
EEC	Fully electrified energy community
EU	European Union
FC	Fuel cell
GEC	Gas-based energy community
HEC	Hydrogen-based energy community
HP	Heat pump
MG	Microgrid
RES	Renewable energy sources
RoCoF	Rate-of-change-of-frequency
VSM	Virtual synchronous machine
Superscripts	
E/G/H/T	Electrical/Gas/Hydrogen/Thermal quantity
Sets	
$\mathcal{D}_m$	Set of all energy conversion devices in EC m
$\mathcal{D}_{d,m}$	Set of devices $d \in \{b, c, e, f, h, \beta, \tau, \hbar\}$ in EC m
$\mathcal{D}_m^C$	Set of all energy conversion devices in EC m that are not storage devices; $\mathcal{D}_m^C = \mathcal{D}_m \backslash \mathcal{D}_m^S$, $\mathcal{D}_m^C \subseteq \mathcal{D}_m$

$\mathcal{D}_m^S$	Set of all energy conversion devices in EC m that are also storage devices; $\mathcal{D}_m^S = \mathcal{D}_m \backslash \mathcal{D}_m^C$, $\mathcal{D}_m^S \subseteq \mathcal{D}_m$
$\mathcal{M}$	Set of ECs, $\mathcal{M} = \{\text{EEC}, \text{GEC}, \text{HEC}\}$, indexed by m
$\mathcal{N}_m$	Set of network nodes in EC m, indexed by n
$\mathcal{T}$	Set of hours in a representative year, indexed by t
Parameters	
$E_d^{\max}$	Maximum state-of-energy of device d
$E_d^{\min}$	Minimum state-of-energy of device d
$L_{n,m,t}^{\mathrm{E}}$	Electric load demand at node n in EC m at time t
$L_{n,m,t}^{\mathrm{T}}$	Heat demand at node n in EC m at time t
$\overline{P}_d^{\max}$, $\underline{P}_d^{\max}$	Maximum input/ouput power of device d
$\overline{P}_d^{\min}$, $\underline{P}_d^{\min}$	Minimum input/output power of device d
$PV_{n,m,t}^{\mathrm{E}}$	PV production at node n in EC m at time t
η_d	Energy conversion efficiency of device d
η_d^{E}	Electricity conversion efficiency of device d
η_d^{T}	Thermal conversion efficiency of device d
η_d^{c}	Charging efficiency of device d
η_d^{d}	Discharging efficiency of device d
π_t^{E}	Electricity price at time t
$\pi^{\text{trans.}}$	Electricity transmission charge
$\pi^{\text{distr.}}$	Electricity distribution charge
π^{G}	Gas price
Variables	
$\overline{p}_{d,m,t}$	Input power of device d in EC m at time t
$\underline{p}_{d,m,t}$	Output power of device d in EC m at time t
$x_{d,m,t}$	Binary variable indicating whether device d in EC m is operational at time t
$x_{d,m,t}^{\mathrm{c}}$	Binary variable indicating whether device d in EC m is charging at time t
$x_{d,m,t}^{\mathrm{d}}$	Binary variable indicating whether device d in EC m is discharging at time t
$z_{d,m,t}$	Binary variable indicating whether device d in EC m has started up at time t
γ_m	Gas volume bought from day-ahead market in EC m
$\overline{\epsilon}_{m,t}$	Electricity volume bought from day-ahead market in EC m at time t
$\underline{\epsilon}_{m,t}$	Electricity volume sold to day-ahead market in EC m at time t

References

1. De Lotto, R.; Micciché, C.; Venco, E.M.; Bonaiti, A.; De Napoli, R. Energy Communities: Technical, Legislative, Organizational, and Planning Features. *Energies* **2022**, *15*, 1731. [CrossRef]
2. Roberts, J.; Frieden, D.; d'Herbemont, S. Energy community definitions. In *Deliverable Developed under the Scope of the COMPILE Project: Integrating Community Power in Energy Islands*; COMPILE Consortium: Novo Mesto, Slovenia, 2019 ; p. H2020.
3. Lowitzsch, J.; Hoicka, C.E.; van Tulder, F.J. Renewable energy communities under the 2019 European Clean Energy Package–Governance model for the energy clusters of the future? *Renew. Sustain. Energy Rev.* **2020**, *122*, 109489. [CrossRef]
4. Frieden, D.; Tuerk, A.; Neumann, C.; d'Herbemont, S.; Roberts, J. *Collective Self-Consumption and Energy Communities: Trends and Challenges in the Transposition of the EU Framework*; COMPILE Consortium: Novo Mesto, Slovenia, 2020.
5. Caramizaru, A.; Uihlein, A. *Energy Communities: An Overview of Energy and Social Innovation*; Publications Office of the European Union: Luxembourg, 2020; Volume 30083.
6. Hrvatski Sabor. Zakon o Tržištu Električne Energije. 2021. Available online: https://narodne-novine.nn.hr/clanci/sluzbeni/2021_10_111_1940.html (accessed on 12 April 2022).
7. Grzanić, M.; Morales, J.M.; Pineda, S.; Capuder, T. Electricity cost-sharing in energy communities under dynamic pricing and uncertainty. *IEEE Access* **2021**, *9*, 30225–30241. [CrossRef]
8. Rebollal, D.; Carpintero-Rentería, M.; Santos-Martín, D.; Chinchilla, M. Microgrid and distributed energy resources standards and guidelines review: Grid connection and operation technical requirements. *Energies* **2021**, *14*, 523. [CrossRef]
9. Tostado-Véliz, M.; Kamel, S.; Hasanien, H.M.; Turky, R.A.; Jurado, F. Optimal energy management of cooperative energy communities considering flexible demand, storage and vehicle-to-grid under uncertainties. *Sustain. Cities Soc.* **2022**, *84*, 104019. [CrossRef]
10. Li, Z.; Xu, Y. Optimal coordinated energy dispatch of a multi-energy microgrid in grid-connected and islanded modes. *Appl. Energy* **2018**, *210*, 974–986. [CrossRef]
11. Zhang, C.; Xu, Y.; Dong, Z.Y. Robustly coordinated operation of a multi-energy micro-grid in grid-connected and islanded modes under uncertainties. *IEEE Trans. Sustain. Energy* **2019**, *11*, 640–651. [CrossRef]

12. Khodaei, A. Microgrid optimal scheduling with multi-period islanding constraints. *IEEE Trans. Power Syst.* **2013**, *29*, 1383–1392. [CrossRef]
13. Shah, P.; Mehta, B. Microgrid optimal scheduling with renewable energy sources considering islanding constraints. *Iran. J. Sci. Technol. Trans. Electr. Eng.* **2020**, *44*, 805–819. [CrossRef]
14. Lee, J.; Lee, S.; Lee, K. Multistage Stochastic Optimization for Microgrid Operation Under Islanding Uncertainty. *IEEE Trans. Smart Grid* **2020**, *12*, 56–66. [CrossRef]
15. Liu, G.; Starke, M.; Xiao, B.; Tomsovic, K. Robust optimisation-based microgrid scheduling with islanding constraints. *IET Gener. Transm. Distrib.* **2017**, *11*, 1820–1828. [CrossRef]
16. Kouhian, F.; Zangeneh, A.; Martí, J.R. Three-based level model to determine optimal scheduling of the MG integrated operation using Benders decomposition. *IET Gener. Transm. Distrib.* **2019**, *13*, 4712–4723. [CrossRef]
17. Kumari, K.K.; Babu, R.S.R. Optimal scheduling of a micro-grid with multi-period islanding constraints using hybrid CFCS technique. In *Evolutionary Intelligence*; Springer: Berlin/Heidelberg, Germany, 2022; pp. 1–20.
18. Lee, S.Y.; Jin, Y.G.; Yoon, Y.T. Determining the optimal reserve capacity in a microgrid with islanded operation. *IEEE Trans. Power Syst.* **2015**, *31*, 1369–1376. [CrossRef]
19. Wu, Y.; Lim, G.J.; Shi, J. Stability-constrained microgrid operation scheduling incorporating frequency control reserve. *IEEE Trans. Smart Grid* **2019**, *11*, 1007–1017. [CrossRef]
20. Liu, G.; Starke, M.; Xiao, B.; Zhang, X.; Tomsovic, K. Microgrid optimal scheduling with chance-constrained islanding capability. *Electr. Power Syst. Res.* **2017**, *145*, 197–206. [CrossRef]
21. Chu, Z.; Zhang, N.; Teng, F. Frequency-Constrained Resilient Scheduling of Microgrid: A Distributionally Robust Approach. *IEEE Trans. Smart Grid* **2021**, *12*, 4914–4925. [CrossRef]
22. Nakiganda, A.M.; Dehghan, S.; Aristidou, P. Enhancing Microgrid Resilience and Survivability under Static and Dynamic Islanding Constraints. In Proceedings of the 2020 IEEE PES Innovative Smart Grid Technologies Europe (ISGT-Europe), The Hague, The Netherlands, 26–28 October 2020; pp. 539–543.
23. Javadi, M.; Gong, Y.; Chung, C. Frequency stability constrained microgrid scheduling considering seamless Islanding. *IEEE Trans. Power Syst.* **2021**, *37*, 306–316. [CrossRef]
24. Wen, Y.; Chung, C.; Liu, X.; Che, L. Microgrid dispatch with frequency-aware islanding constraints. *IEEE Trans. Power Syst.* **2019**, *34*, 2465–2468. [CrossRef]
25. Nakiganda, A.M.; Van Cutsem, T.; Aristidou, P. Microgrid Operational Optimization with Dynamic Voltage Security Constraints. In Proceedings of the 2021 IEEE Madrid PowerTech, Madrid, Spain, 28 June–2 July 2021; pp. 1–6.
26. Vahedipour-Dahraie, M.; Reza Najafi, H.; Anvari-Moghaddam, A.; Guerrero, J.M. Optimal scheduling of distributed energy resources and responsive loads in islanded microgrids considering voltage and frequency security constraints. *J. Renew. Sustain. Energy* **2018**, *10*, 025903. [CrossRef]
27. Kiliç, H.; Khaki, B.; Gumuş, B.; Yilmaz, M.; Asker, M.E. Stability analysis of islanded microgrid with EVs. In Proceedings of the 2018 Smart Grid Conference (SGC), Kurdistan, Iran, 28–29 November 2018; pp. 1–5.
28. Mazidi, M.; Rezaei, N.; Ardakani, F.J.; Mohiti, M.; Guerrero, J.M. A hierarchical energy management system for islanded multi-microgrid clusters considering frequency security constraints. *Int. J. Electr. Power Energy Syst.* **2020**, *121*, 106134. [CrossRef]
29. Ebrahimi, M.R.; Amjady, N.; Hatziargyriou, N.D. Microgrid Operation Optimization Considering Transient Stability Constraints: A New Bidirectional Stochastic Adaptive Robust Approach. *IEEE Syst. J.* **2021**, *16*, 5663–5674. [CrossRef]
30. Nakiganda, A.M.; Dehghan, S.; Markovic, U.; Hug, G.; Aristidou, P. A Stochastic-Robust Approach for Resilient Microgrid Investment Planning Under Static and Transient Islanding Security Constraints. *IEEE Trans. Smart Grid* **2022**, *13*, 1774–1788. [CrossRef]
31. Ortiz-Villalba, D.; Llanos, J.; Munoz-Jadan, Y.; Moreno, R.; Rahman, C.; Pal, B.C. Optimizing System Operation with Nadir Considerations via Simulations of Detailed System Dynamic Responses. In Proceedings of the 22nd Power Systems Computation Conference, Porto, Portugal, 27 June–1 July 2022.
32. Zhang, Y.; Chen, C.; Liu, G.; Hong, T.; Qiu, F. Approximating trajectory constraints with machine learning–microgrid islanding with frequency constraints. *IEEE Trans. Power Syst.* **2020**, *36*, 1239–1249. [CrossRef]
33. Gurobi Optimization, L.L.C. *Gurobi Optimizer Reference Manual*; Gurobi Optimization, LLC: Beaverton, OR, USA, 2012.
34. Rocabert, J.; Luna, A.; Blaabjerg, F.; Rodriguez, P. Control of power converters in AC microgrids. *IEEE Trans. Power Electron.* **2012**, *27*, 4734–4749. [CrossRef]
35. Hovsapian, R. Role of Electrolyzers in Grid Services. 2017. Available online: https://www.energy.gov/sites/prod/files/2017/06/f34/fcto_may_2017_h2_scale_wkshp_hovsapian.pdf (accessed on 21 May 2023).
36. Garcia Suarez, V. Exploitation of Power-to-Gas for Ancillary Services Provision (within the Context of Synergy Action TSO 2020). Master's Thesis, TU Delft, Delft, The Netherlands, 2018.
37. Veerakumar, N.; Ahmad, Z.; Adabi, M.E.; Torres, J.R.; Palensky, P.; van der Meijden, M.; Gonzalez-Longatt, F. Fast active power-frequency support methods by large scale electrolyzers for multi-energy systems. In Proceedings of the 2020 IEEE PES Innovative Smart Grid Technologies Europe (ISGT-Europe), The Hague, The Netherlands, 26–28 October 2020; pp. 151–155.
38. Tuinema, B.W.; Adabi, E.; Ayivor, P.K.; Suárez, V.G.; Liu, L.; Perilla, A.; Ahmad, Z.; Torres, J.L.R.; van der Meijden, M.A.; Palensky, P. Modelling of large-sized electrolysers for real-time simulation and study of the possibility of frequency support by electrolysers. *IET Gener. Transm. Distrib.* **2020**, *14*, 1985–1992. [CrossRef]

39. Guilbert, D.; Vitale, G. Dynamic emulation of a pem electrolyzer by time constant based exponential model. *Energies* **2019**, *12*, 750. [CrossRef]
40. Dozein, M.G.; De Corato, A.M.; Mancarella, P. Fast Frequency Response Provision from Large-Scale Hydrogen Electrolyzers Considering Stack Voltage- Current Nonlinearity. In Proceedings of the 2021 IEEE Madrid PowerTech, Madrid, Spain, 14 July 2021; pp. 1–6.
41. Dozein, M.G.; Jalali, A.; Mancarella, P. Fast frequency response from utility-scale hydrogen electrolyzers. *IEEE Trans. Sustain. Energy* **2021**, *12*, 1707–1717. [CrossRef]
42. Chiesa, N.; Korpås, M.; Kongstein, O.; Ødegård, A. Dynamic Control of an Electrolyser for Voltage Quality Enhancement. 2011. Available online: https://www.ipstconf.org/papers/Proc_IPST2011/11IPST072.pdf (accessed on 21 May 2023).
43. Alshehri, F. Ancillary services from Hydrogen Based Technologies to Support Power System Frequency Stability. Master's Thesis, TU Delft, Delft, The Netherlands, 2018.
44. Alshehri, F.; Suárez, V.G.; Perilla, A.; Adabi, M.E.; Rueda Torres, J.L.; van der Meijden, M.A. Generic Modelling of PEM Technologies for Power System Stability Studies Based on PowerFactory. In *Modelling and Simulation of Power Electronic Converter Dominated Power Systems in PowerFactory*; Springer: Berlin/Heidelberg, Germany, 2021; pp. 269–283.
45. Marquezini, D.; Ramos, D.; Machado, R.; Farret, F. Interaction between proton exchange membrane fuel cells and power converters for AC integration. *IET Renew. Power Gener.* **2008**, *2*, 151–161. [CrossRef]
46. Daud, W.; Rosli, R.; Majlan, E.; Hamid, S.; Mohamed, R.; Husaini, T. PEM fuel cell system control: A review. *Renew. Energy* **2017**, *113*, 620–638. [CrossRef]
47. Pathapati, P.; Xue, X.; Tang, J. A new dynamic model for predicting transient phenomena in a PEM fuel cell system. *Renew. Energy* **2005**, *30*, 1–22. [CrossRef]
48. Wöhr, M.; Bolwin, K.; Schnurnberger, W.; Fischer, M.; Neubrand, W.; Eigenberger, G. Dynamic modelling and simulation of a polymer membrane fuel cell including mass transport limitation. *Int. J. Hydrogen Energy* **1998**, *23*, 213–218. [CrossRef]
49. Saadi, A.; Becherif, M.; Hissel, D.; Ramadan, H.S. Dynamic modeling and experimental analysis of PEMFCs: A comparative study. *Int. J. Hydrogen Energy* **2017**, *42*, 1544–1557. [CrossRef]
50. Pukrushpan, J.T. Modeling and Control of PEM Fuel Cell Systems and Fuel Processors. Ph.D. Thesis, University of Michigan, Ann Arbor, MI, USA, 2003.
51. Taieb, A.; Mukhopadhyay, S.; Al-Othman, A. Dynamic model of a proton-exchange membrane fuel cell using equivalent electrical circuit. In Proceedings of the 2019 Advances in Science and Engineering Technology International Conferences (ASET), Dubai, United Arab Emirates, 26 March–10 April 2019; pp. 1–4.
52. Larminie, J.; Dicks, A.; McDonald, M.S. *Fuel Cell Systems Explained*; Wiley: Chichester, UK, 2003; Volume 2.
53. Khan, M.; Iqbal, M. Modelling and analysis of electro-chemical, thermal, and reactant flow dynamics for a PEM fuel cell system. *Fuel Cells* **2005**, *5*, 463–475. [CrossRef]
54. Lee, J.; Cho, B. A dynamic model of a PEM fuel cell system. In Proceedings of the 2009 Twenty-Fourth Annual IEEE Applied Power Electronics Conference and Exposition, Washington, DC, USA, 15–19 February 2009; pp. 720–724.
55. Alshehri, F.; Torres, J.R.; Perilla, A.; Tuinema, B.W.; van der Meijden, M.A.; Palensky, P.; Gonzalez-Longatt, F. Generic model of PEM fuel cells and performance analysis in frequency containment period in systems with decreased inertia. In Proceedings of the 2019 IEEE 28th International Symposium on Industrial Electronics (ISIE), Vancouver, BC, Canada, 12–14 June 2019; pp. 1810–1815.
56. Ge, Y.; Zhao, Y.; Li, H.; Tan, J.; Chen, H. Virtual Synchronous Control for Fuel Cell Power Generation System. *IOP Conf. Ser. Earth Environ. Sci.* **2020**, *610*, 012007. [CrossRef]
57. Hatziadoniu, C.; Lobo, A.; Pourboghrat, F.; Daneshdoost, M. A simplified dynamic model of grid-connected fuel-cell generators. *IEEE Trans. Power Deliv.* **2002**, *17*, 467–473. [CrossRef]
58. Barać, B.; Krpan, M.; Capuder, T.; Kuzle, I. Modeling and Initialization of a Virtual Synchronous Machine for Power System Fundamental Frequency Simulations. *IEEE Access* **2021**, *9*, 160116–160134. [CrossRef]
59. *Battery Energy Storing Systems, DIg SILENT Power Factory, Application Example*; Technical Report; DIgSILENT GmbH: Gomaringen, Germany, 2010.
60. Barać, B.; Kostelac, M.; Pavić, I.; Capuder, T.; Grašo, J.; Marušić, A.; Koledić, T.; Barišin, J. Modelling and Evaluating Capability of Battery Storage Systems to Provide Extreme Event Services to the DSO: Case Study of Croatia. In Proceedings of the 2022 IEEE 21st Mediterranean Electrotechnical Conference (MELECON), Palermo, Italy, 14–16 June 2022; pp. 34–39.
61. Capuder, T.; Kostelac, M.; Krpan, M.; Pavić, I. Multi-energy microgrid ability to provide flexibility services to the system operator and security of supply to end-users. In Proceedings of the 2020 International Conference on Smart Energy Systems and Technologies (SEST), Istanbul, Turkey, 7–9 September 2020; pp. 1–6.
62. Huang, L.; Xin, H.; Wang, Z.; Wu, K.; Wang, H.; Hu, J.; Lu, C. A virtual synchronous control for voltage-source converters utilizing dynamics of DC-link capacitor to realize self-synchronization. *IEEE J. Emerg. Sel. Top. Power Electron.* **2017**, *5*, 1565–1577. [CrossRef]
63. Markovic, U. Towards Reliable Operation of Converter-Dominated Power Systems: Dynamics, Optimization and Control. Ph.D. Thesis, ETH Zurich, Zurich, Switzerland, 2020.
64. Shankar, R.; Kundur, P. *Power SYSTEM Stability and Control II*; McGraw-Hill Books: New York, NY, USA, 1994; p. 581.
65. Kostelac, M.; Herenčić, L.; Capuder, T. Planning and Operational Aspects of Individual and Clustered Multi-Energy Microgrid Options. *Energies* **2022**, *15*, 1317. [CrossRef]

66. Pflugradt, N.; Muntwyler, U. Synthesizing residential load profiles using behavior simulation. *Energy Procedia* **2017**, *122*, 655–660. CISBAT 2017 International ConferenceFuture Buildings & Districts—Energy Efficiency from Nano to Urban Scale. [CrossRef]
67. Pfenninger, S.; Staffell, I. Long-term patterns of European PV output using 30 years of validated hourly reanalysis and satellite data. *Energy* **2016**, *114*, 1251–1265. [CrossRef]
68. Croatian Energy Exchange. Available online: https://www.cropex.hr/en/ (accessed on 21 May 2023).
69. Open Energy Data Initiative (OEDI). Available online: https://data.openei.org/ (accessed on 21 May 2023).
70. Spot Market Data | CEGH VTP. Available online: https://www.powernext.com/spot-market-data (accessed on 21 May 2023).